



# Fabrication, characterization and mechanism of a novel Z-scheme $\text{Ag}_3\text{PO}_4/\text{NG/polyimide}$ composite photocatalyst for microcystin-LR degradation

Qiang Guo<sup>a</sup>, Hui Li<sup>a</sup>, Qian Zhang<sup>a</sup>, Yanlin Zhang<sup>a,b,\*</sup>

<sup>a</sup> School of Chemistry and Environment, South China Normal University, Guangzhou, 510006, China

<sup>b</sup> Key Laboratory of Theoretical Chemistry of Environment, Ministry of Education, South China Normal University, Guangzhou, 510006, China



## ARTICLE INFO

### Keywords:

Silver orthophosphate  
Polyimide  
Nitrogen-doped graphene  
Photocatalytic degradation  
Microcystins

## ABSTRACT

In recent years, the frequent eutrophication of water bodies around the world has led to the accumulation of microcystins (MC-LR) in water bodies, causing great harm to humans and aquatic organisms. In this study, a Z-scheme  $\text{Ag}_3\text{PO}_4/\text{NG/PI}$  composite photocatalyst was fabricated by using silver orthophosphate, nitrogen-doped graphene and polyimide for photocatalytic degradation of MC-LR under visible light irradiation. The structure, morphology and optical properties of  $\text{Ag}_3\text{PO}_4/\text{NG/PI}$  were characterized by XRD, SEM, TEM, XPS, FT-IR, BET, and UV-vis DRS. The degradation ratio of MC-LR by  $\text{Ag}_3\text{PO}_4/\text{NG/PI}$  photocatalysts was higher (up to 94.4%) than that of pure  $\text{Ag}_3\text{PO}_4$  for MC-LR degradation within 10 h under visible light irradiation, and the kinetic constant over  $\text{Ag}_3\text{PO}_4/\text{NG/PI}$  was ~7 times of pure  $\text{Ag}_3\text{PO}_4$ . Based on the results of Liquid Chromatography–Mass Spectrometry (LC-MS), the possible degradation pathways of MC-LR were proposed. Photoelectrochemistry measurement (the photocurrent response, electrochemical impedance spectroscopy and Mott–Schottky plots), radical trapping experiment, electron spin resonance test, PL spectroscopy and analysis of band gap have revealed that the photocatalysis of  $\text{Ag}_3\text{PO}_4/\text{NG/PI}$  follows the Z-scheme mechanism, which can not only promote the separation and migration of photogenerated carriers to reduce re-combination, but also maintain a strong redox capacity. Meanwhile, the stability of  $\text{Ag}_3\text{PO}_4/\text{NG/PI}$  photocatalyst is greatly improved because the photogenerated electrons ( $e^-$ ) of  $\text{Ag}_3\text{PO}_4$  are migrated to NG to suppress the photo-corrosion of  $\text{Ag}_3\text{PO}_4$ .

## 1. Introduction

In recent years, cyanobacteria bloom in freshwater is becoming more and more serious as a result of the increasing water eutrophication in the world. When cyanobacteria happens, harmful algae such as *Microcystis aeruginosa* produces a series of cyano toxins-microcystins (MCs) [1]. Microcystin (MC-LR) is the most harmful among the various algal toxins, posing a serious threat to water ecological security and human health [2]. Therefore, it is imperative to control the concentration of algal toxins in water and to find effective degradation methods. MC-LR molecules with cyclic structures and specific amino acids are very stable and extremely difficult to be eliminated by conventional chemical treatment [3] with the result that the photocatalytic technology has attracted increasing attentions due to its unique properties such as low energy consumption, high efficiency and low pollution [4–9].

$\text{Ag}_3\text{PO}_4$  with a quantum efficiency of over 90% is recognized as a promising visible-light photocatalyst [10–13]. However, this silver-containing photocatalyst usually experiences photo-corrosion under

visible light irradiation, which damages its photocatalytic activity so as to limit its industrial application. To avoid this situation, it is necessary to rapidly migrate photogenerated electrons from  $\text{Ag}_3\text{PO}_4$  surface to acceptor material before  $\text{Ag}^+$  is reduced to metallic  $\text{Ag}^\circ$  [14]. As previously reported, the strategy of  $\text{Ag}_3\text{PO}_4$  coupling with semiconductors to form heterojunction can be used to construct new composite to improve its photoactivity and photostability, such as  $\text{AgX}$  ( $X = \text{Cl}, \text{Br}$  and  $\text{I}$ ) [15],  $\text{ZnO}$  [16], graphene [17],  $\text{g-C}_3\text{N}_4$  [18],  $\text{TiO}_2$  [19],  $\text{Ag}_2\text{S}$  [20],  $\text{AuNRs}$  [21], 3DOM- $\text{SrTiO}_3/\text{Ag}$  [22] and  $\text{ZnO}$  [23].

Recently, the Z-scheme photocatalytic principle, which simulates the natural photosynthesis, has been widely used in environmental aspects [24]. Z-scheme type photocatalytic materials tend to have stronger redox ability than conventional heterojunction nanocomposite photocatalysts. Z-scheme photocatalytic composite materials can not only ensure a wide range of light response, but also improve the ability of redox, which shows a wider range of applications [25]. Very recently, a variety of Z-scheme photocatalysts have been reported, such as  $\text{TiO}_2/\text{rGO}/\text{WO}_3$  [24],  $\text{Ag}_2\text{CrO}_4/\text{GO}$  [26],  $\text{TNT}/\text{CdS}/\text{GR}$  [27],  $\text{g-C}_3\text{N}_4/\text{Ag}/\text{Ag}_3\text{PO}_4$  [28],  $\text{CuGaS}_2/\text{Pt}/\text{RGO-TiO}_2$  [29],  $\text{Ru}/(\text{SrTiO}_3:\text{Rh})-(\text{BiVO}_3)$

\* Corresponding author at: School of Chemistry and Environment, South China Normal University, Guangzhou, 510006, China.  
E-mail address: [zhangyl@scnu.edu.cn](mailto:zhangyl@scnu.edu.cn) (Y. Zhang).

( $\text{Fe}^{3+}/\text{Fe}^{2+}$ ) [30]. In the solid-state Z-scheme photocatalytic reaction system, the charge transmitted by the interface contact can shorten the transmission distance and reduce the chance of the side reaction, thus the photocatalytic efficiency are improved.

In this study,  $\text{Ag}_3\text{PO}_4$ , nitrogen-doped graphene (NG) and polyimide (PI) were selected to construct the Z-scheme photocatalyst, which exhibited enhanced photocatalytic activity and attracted increasing attention due to its unique properties [25,31]. Reduced graphene (rGO) as an excellent solid electron mediator for photocatalyst has the advantages of large specific surface area, strong adsorption capacity, fast electron transport, high conductivity, good chemical and thermal stability [30,32,33]. Because its conductivity cannot be completely controlled like conventional semiconductors because of the lack of limited band gap [34], nitrogen doping into the rGO can increase the free carrier density of graphene by changing the electronic properties of graphene [35]. For example, NG/TiO<sub>2</sub> [36] and AgNPs/NG [37] have demonstrated that the introduction of NG can bring desired electronic characteristics to graphene, which thus improves the photocatalytic performance of photocatalysts. Polyimide, a kind of conjugated polymer, has been used to improve the photocatalytic performance of semiconductors because of its ease of preparation, environmental stability, and high conductivity after doping [8,38,39]. In addition, the introduction of PI can reduce the band gap to improve the absorption wavelength of the composite, which is beneficial for the enhancement of the photon absorption efficiency of the composite.

Herein, the as-prepared  $\text{Ag}_3\text{PO}_4/\text{NG}/\text{PI}$  composite was employed to degrade microcystin (MC-LR) with the aid of visible light irradiation in which the photocatalysis of  $\text{Ag}_3\text{PO}_4/\text{NG}/\text{PI}$  composite abided by the Z-scheme mechanism possessing high charge separation efficiency and strong redox capacity [31,40]. Furthermore, the photo-corrosion of  $\text{Ag}_3\text{PO}_4$  is effectively suppressed by introducing NG as an electron transfer mediator. The degradation mechanism and pathways of MC-LR in  $\text{Ag}_3\text{PO}_4/\text{NG}/\text{PI}$  photocatalytic system were explored.

## 2. Experimental

### 2.1. Chemicals

$\text{AgNO}_3$  was purchased from Sinopharm Chemical Reagent Co., Melamine (MA), trifluoroacetic acid (TFA) and pyromellitic anhydride (PMDA) were purchased from Shanghai Macklin Biochemical Co., DuPont 5% nafton solution was purchased from Cool Seoul Chemical Technology (Beijing) Co., Acetonitrile and methanol were purchased from Tianjin Kermel Chemical Reagent Co., 5-dimethyl-1-pyrroline-N-oxide (DMPO), disodium ethylenediaminetetraacetic (EDTA-2Na), sodium dodecahydrate ( $\text{Na}_3\text{PO}_4 \cdot 12\text{H}_2\text{O}$ ), formic acid, *t*-butyl alcohol (TBA), Polyethylene glycol 400 (PEG-400), disodium hydrogen phosphate dodecahydrate ( $\text{Na}_2\text{HPO}_4 \cdot 12\text{H}_2\text{O}$ ) and benzoquinone (BQ) were purchased from Aladdin Co. MC-LR (0.5 mg, 96.4% purity) was purchased as a solid from Calbiochem (Gibbstown, NJ) and stored in a freezer at  $-20^\circ\text{C}$ . 1 mL autoclaved Milli-Q water was added to produce 500 mg L<sup>-1</sup> of MC-LR stock solution, MC-LR solid was dissolved in two days and vortexed for 2 min each day.

### 2.2. Synthesis of $\text{Ag}_3\text{PO}_4$

0.01 mol  $\text{AgNO}_3$  was dissolved in 100 mL deionized water, followed by adding 100 mL 8 g L<sup>-1</sup> PEG-400 solution. Then the mixture was stirred vigorously for 20 min, 100 mL 0.05 mol L<sup>-1</sup>  $\text{Na}_2\text{HPO}_4$  solution was added drop by drop. After stirring in the dark for 2 h, the collected  $\text{Ag}_3\text{PO}_4$  precipitate was washed with distilled water and absolute ethanol and subsequently dried at 60 °C for 12 h.

### 2.3. Synthesis of NG

NG was synthesized via hydrazine steaming process [41]. Briefly,

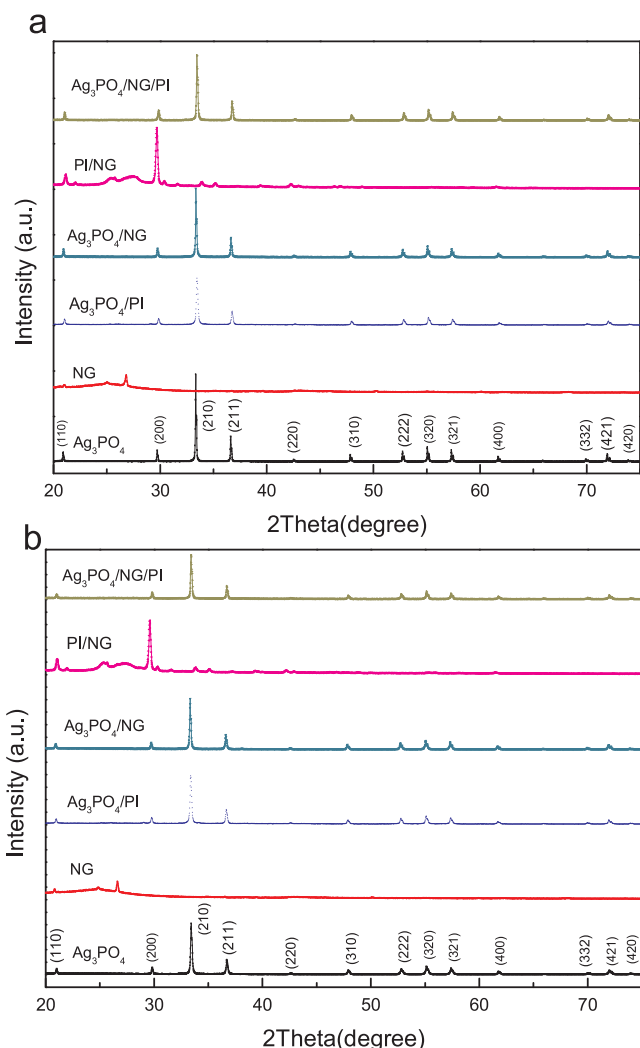


Fig. 1. XRD patterns of synthesized samples (a) before degradation, and (b) after degradation.

GO was firstly prepared by the Hummers' method. Subsequently the as-synthesized GO was placed on the silica griddle of a sand core funnel, followed by putting in the reaction kettle equipped with 5 mL 80% hydrazine hydrate, and then sealed it in oven at 100 °C for 4 h. After completion of the reaction, the mixture was cooled to room temperature, and the collected NG was dried at 60 °C for 12 h.

### 2.4. Synthesis of PI

1.26 g MA and 2.18 g PMDA (molar ratio 1:1) were mixed and ground evenly in the agate mortar. The mixture was then placed in a capped porcelain boat (semi-closed system), raised to 325 °C at a rate of 7 °C min<sup>-1</sup> and maintained for 4 h. The obtained yellow solid was ground uniformly into a powder, washed with 50 °C water to remove residual monomer and dried for use.

### 2.5. Fabrication of $\text{Ag}_3\text{PO}_4/\text{NG}$ , $\text{PI}/\text{NG}$ , $\text{Ag}_3\text{PO}_4/\text{PI}$ and $\text{Ag}_3\text{PO}_4/\text{NG}/\text{PI}$

NG was added to the appropriate amount of isopropanol for ultrasonic dispersion, then a certain amount of  $\text{Ag}_3\text{PO}_4$  was added into the above solution in proportion. Then the suspension was ultrasonicated for 3 h, vigorously stirred for 6 h, and finally dried in a vacuum oven at 60 °C for 12 h. PI/NG,  $\text{Ag}_3\text{PO}_4/\text{PI}$  and  $\text{Ag}_3\text{PO}_4/\text{NG}/\text{PI}$  were all prepared by the above method. When preparing  $\text{Ag}_3\text{PO}_4/\text{NG}/\text{PI}$ , the first to be added to isopropanol was the prepared  $\text{Ag}_3\text{PO}_4/\text{NG}$ .

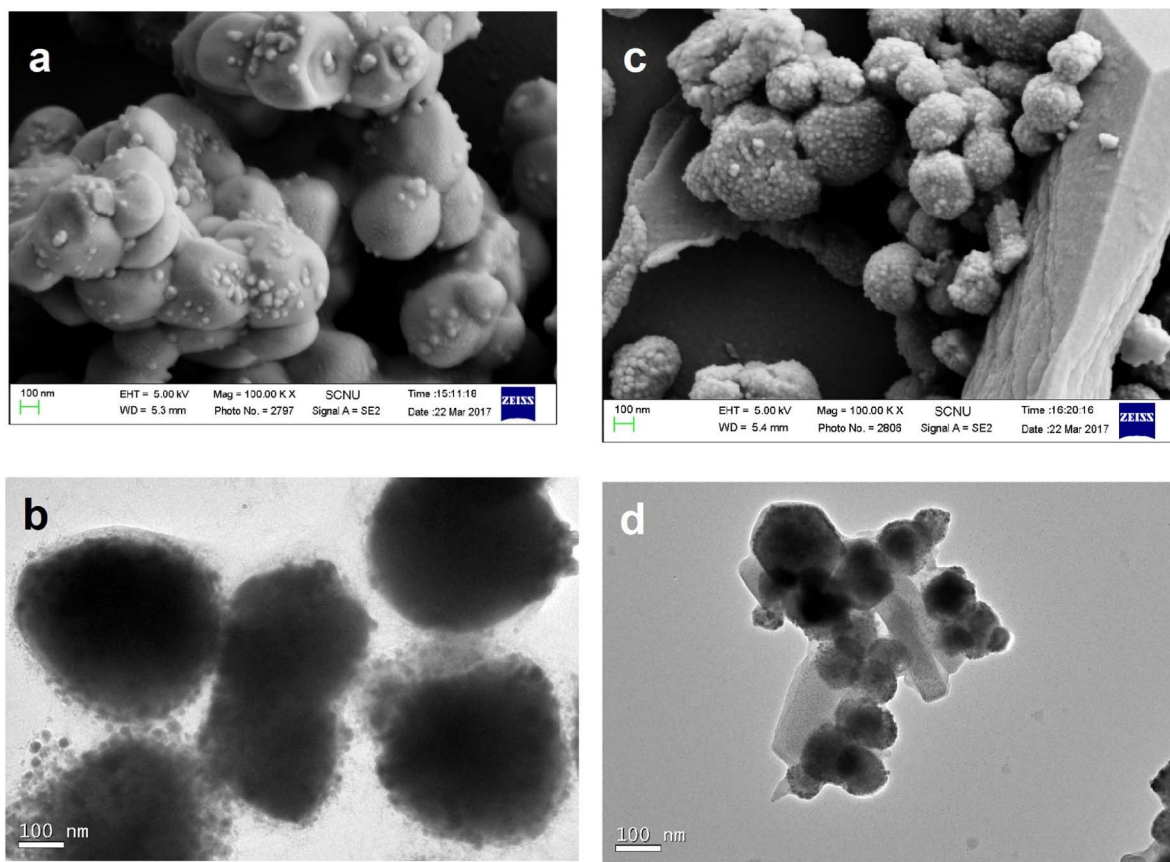


Fig. 2. SEM images of (a)  $\text{Ag}_3\text{PO}_4$ , (c)  $\text{Ag}_3\text{PO}_4/\text{NG/PI}$ , and TEM images of (b)  $\text{Ag}_3\text{PO}_4$ , (d)  $\text{Ag}_3\text{PO}_4/\text{NG/PI}$ .

## 2.6. Characterization

The crystal structure of the samples was determined by powder X-ray diffraction (XRD, Bruker D8 Advance) with  $\text{Cu K}\alpha$  radiation ( $\lambda = 1.5406 \text{ \AA}$ ) in the range of  $20 = 20\text{--}75^\circ$  at 40 kV. The morphology and structure of the synthesized samples were observed by transmission electron microscopy (TEM, JEM-2100HR) and scanning electron microscopy (SEM, ZEISS Ultra 55). The functional groups of the samples were characterized by X-ray photoelectron spectroscopy (XPS, ESCALab250Xi). The Fourier transform infrared spectra (FT-IR) of the samples were recorded on an IR Vertex70 (FT-IR) spectrometer. The UV-vis diffuse reflectance spectra (DRS) of the samples were obtained with a UV-2600 UV-vis-NIR spectrophotometer (Shimadzu UV-2600) equipped with an integrating sphere in the range of 200–800 nm, and  $\text{BaSO}_4$  was used as a reflectance standard. Photoluminescence spectra (PL spectra) of the samples were carried out on an F-2700 fluorescence spectrophotometer (Hitachi, Japan) using a Xenon lamp as the excitation source with an excitation wavelength of 260 nm. Electron spin resonance signals of spin trapped paramagnetic materials with DMPO were recorded with a BrukerElexsys 580 (sensitivity 3000 with weak pitch standard sample) spectrometer.

## 2.7. Photoelectrochemistry measurement

The photocurrent response was measured by CHI660E electrochemical workstation (Chenhua Instruments, Shanghai, China) with a xenon light source (150 W) equipped with an infrared cutoff filter (UVIRCUT400,  $\lambda > 400 \text{ nm}$ ). The measurement was conducted in a conventional three-electrode cell system. Namely, a Pt electrode was employed as the counter electrode, an  $\text{Ag}/\text{AgCl}$  electrode (3 M KCl) as the reference electrode, and the photocatalyst deposited on FTO glass as the working electrode.  $\text{Na}_3\text{PO}_4$  (0.02 M) was used as the electrolyte

solution, and the intermittent illumination time was set at 20 s. After the measurement, the ratio of photocurrent to irradiation area ( $1 \text{ cm}^2$ ) was taken as the optical density  $J$  ( $\mu\text{A cm}^{-2}$ ) and the  $J$ -t curve was plotted. The preparation of the working electrode was as follows: FTO glass ( $1 \times 2 \text{ cm}$ ) was firstly sonicated with acetone, ethanol and water for 15 min, then rinsed with deionized water for three times, and dried in a drying oven. 10 mg of photocatalyst was ultrasonically dispersed in 0.1 ml of ethanol, 2  $\mu\text{L}$  of Nafion solution (5 wt.%) and the suspension was ultrasound for 5 min. Then 25  $\mu\text{L}$  of slurry was sucked with a pipette into the FTO surface (area of  $1 \text{ cm}^2$ ), dried in a fume hood for 30 min, and transferred to a vacuum oven at 60 °C for 12 h to ensure that photocatalytic material was in close contact with the FTO glass. In addition, electrochemical impedance spectroscopy Nyquist plots (EIS) and Mott-Schottky plots (a frequency of 1 kHz) were measured using  $\text{Na}_2\text{SO}_4$  as electrolyte solution (0.1 M, pH = 6.8).

## 2.8. Analysis of the MC-LR concentration

High-performance liquid chromatography (HPLC, Shimadzu, LC10A, with a SPD-10AV UV detector) equipped with a C18 Discovery (Supelco) column (150 mm  $\times$  2.1 mm, 5.0  $\mu\text{m}$  particle size) was used to determine the concentration of MC-LR over time. Both acetonitrile (A) and water (B) contained 0.05% TFA. The mobile phase consisted of 60% A and 40% B. Detection wavelength was set at 238 nm, the flowrate was set to 0.2  $\text{mL min}^{-1}$ , the injection volume was 20  $\mu\text{L}$ , and the column temperature was maintained at 40 °C [42]. MC-LR was detected after  $\sim 5.8$  min elution under these conditions. A Shimadzu TOC 5000 analyzer was used to measure TOC.

## 2.9. LC-MS analysis

MC-LR intermediates identification was carried out using an Agilent

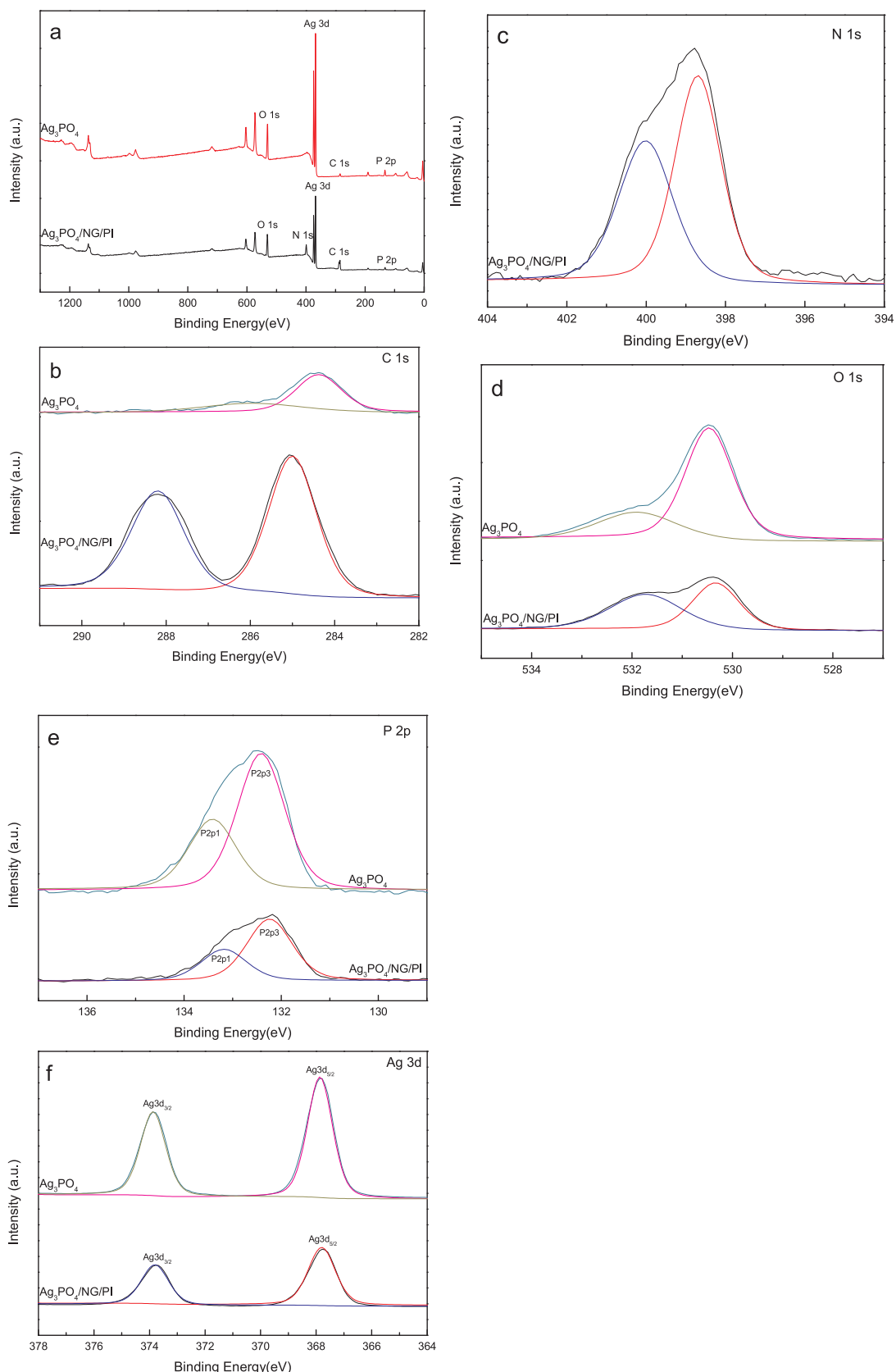


Fig. 3. The XPS spectra of (a) survey spectra, (b) C 1s, (d) O 1s, (e) P 2p, (f) Ag3d of Ag<sub>3</sub>PO<sub>4</sub> and Ag<sub>3</sub>PO<sub>4</sub>/NG/PI, and (c) N 1s spectrum of Ag<sub>3</sub>PO<sub>4</sub>/NG/PI, respectively.

1100 Binary Liquid Chromatograph equipped with a Waters Xterra MS C8 Column (150 mm × 2.1 mm, 3.5 μm particle size). The injection volume was 10 μL, the capillary temperature was 300 °C, and the

flowrate was 0.3 mL min<sup>-1</sup>. Positive ion electrospray ionization (ESI), a Scientific LTQ XL ion trap mass spectrometer and full-scan mode (*m/z* 50–1200) were used for the LC–MS instrument control and data

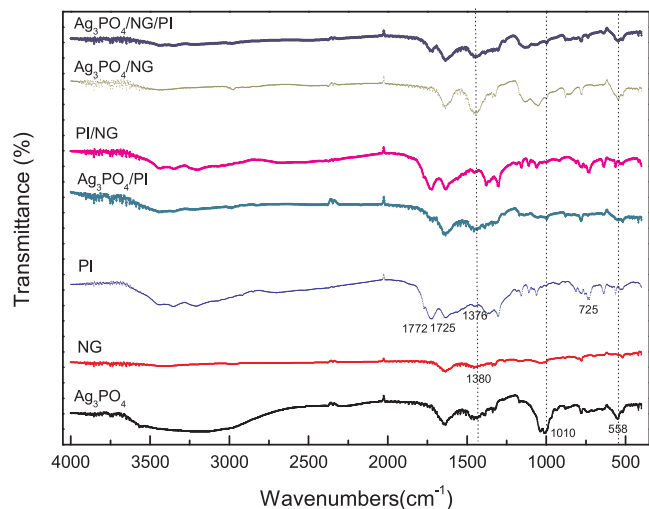


Fig. 4. FT-IR spectra of  $\text{Ag}_3\text{PO}_4$ , NG, PI, PI/NG,  $\text{Ag}_3\text{PO}_4/\text{PI}$ ,  $\text{Ag}_3\text{PO}_4/\text{NG}$  and  $\text{Ag}_3\text{PO}_4/\text{NG/PI}$ .

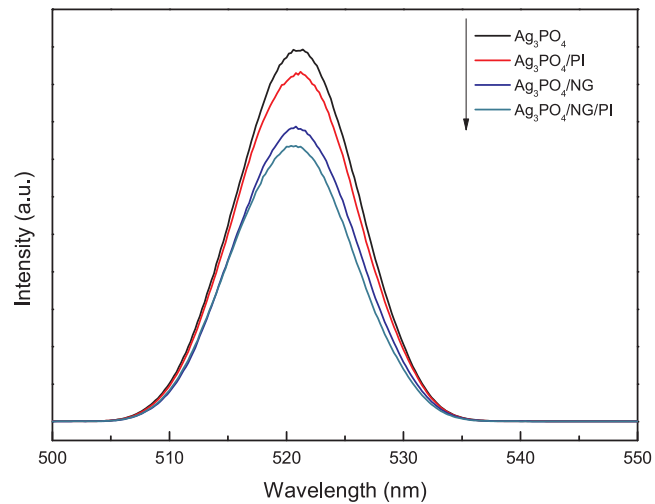


Fig. 6. The photoluminescence spectra of the prepared photocatalysts.

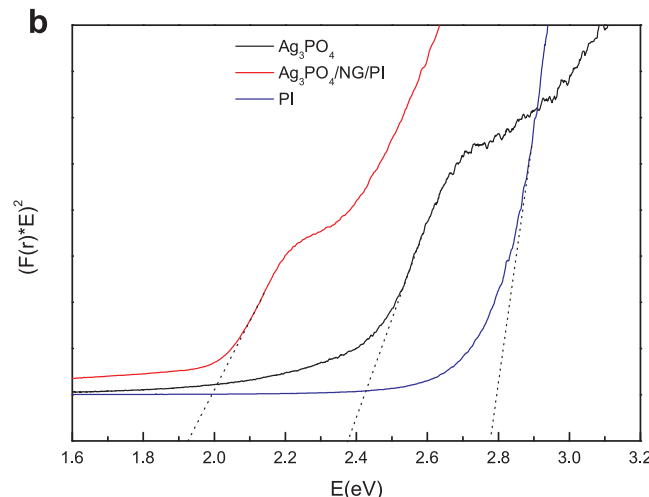
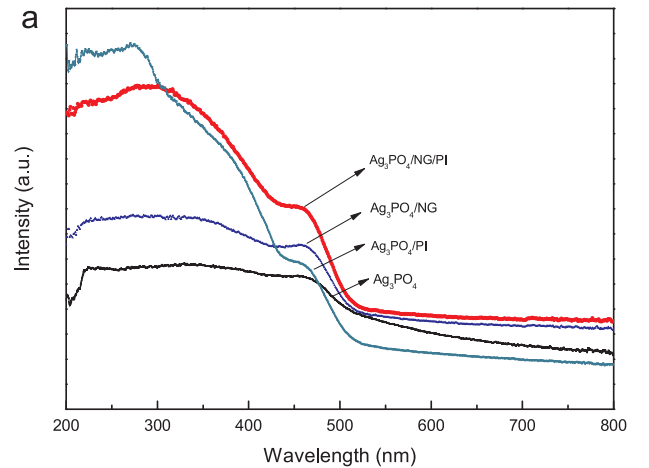


Fig. 5. UV-vis absorbance spectra of synthesized samples (a), and estimated band gap of  $\text{Ag}_3\text{PO}_4$  and  $\text{Ag}_3\text{PO}_4/\text{NG/PI}$  (b).

analysis. The mobile phase consisted of high-purity water (A) and methanol (B), and both A and B contained 0.1% formic acid. The gradient elution procedure was 15–25% B (10 min), followed by an increase to 40% B (10 min), and finally a 15 min linear ramp to 80% B [43].

## 2.10. Photocatalytic experiments

Photocatalytic activities of the as-prepared samples were evaluated by the MC-LR degradation in a photochemical reaction instrument (BL-GHX-V, Bilang Co., China) equipped with a 250 W xenon lamp and a UV cutoff filter ( $\lambda > 420$  nm). In this experiment, 5 mg prepared photocatalyst was added to 10 mL 5 mg L<sup>-1</sup> MC-LR aqueous solution. The solution was magnetically stirred in the dark for 1 h to achieve the adsorption-desorption equilibrium. Afterward, the xenon lamp was adjusted to 250 W to irradiate the suspension. 0.6 mL aliquots were taken at a given interval time and filtered with a 0.22  $\mu\text{m}$  filter membrane. HPLC was adopted for analysis of the residual concentration of MC-LR at different time and the degradation curve of MC-LR was plotted.

## 3. Results and discussion

### 3.1. Characterization

Fig. 1 shows the XRD patterns of  $\text{Ag}_3\text{PO}_4$ , NG,  $\text{Ag}_3\text{PO}_4/\text{PI}$ ,  $\text{Ag}_3\text{PO}_4/\text{NG}$  and  $\text{Ag}_3\text{PO}_4/\text{NG/PI}$  before and after degradation. Herein,  $\text{Ag}_3\text{PO}_4/\text{NG/PI}$  is a proportionally optimized photocatalytic composite (the ratio of NG to  $\text{Ag}_3\text{PO}_4$  is 0.8 wt.%, and the ratio of PI to  $\text{Ag}_3\text{PO}_4$  is 25 wt.%). All the crystal facets (110), (200), (210), (211), (310), (320) of  $\text{Ag}_3\text{PO}_4$  indicate that the synthesized  $\text{Ag}_3\text{PO}_4$  is the body-centered-cubic crystal structure, and can be indexed to the cubic structure of  $\text{Ag}_3\text{PO}_4$  (JCPDF 06-0505). The (210) crystal plane of  $\text{Ag}_3\text{PO}_4$  crystal corresponds to the diffraction peak at  $2\theta = 33.3^\circ$  in the XRD pattern. It is noted that the XRD pattern of  $\text{Ag}_3\text{PO}_4/\text{PI}$ ,  $\text{Ag}_3\text{PO}_4/\text{NG}$  and  $\text{Ag}_3\text{PO}_4/\text{NG/PI}$  has the same peak shape and position as pure  $\text{Ag}_3\text{PO}_4$ , but the peak diffraction intensities of  $\text{Ag}_3\text{PO}_4/\text{PI}$  and  $\text{Ag}_3\text{PO}_4/\text{NG}$  are weaker than that of  $\text{Ag}_3\text{PO}_4/\text{NG/PI}$ . Therefore, the triple composite photocatalyst is more effective than the binary composite photocatalyst to protect the original crystal structure of  $\text{Ag}_3\text{PO}_4$  from being damaged. The diffraction intensities of the corresponding peaks of the photocatalysts after degradation are slightly weakened, but they remain basically unchanged, indicating the good stability of the photocatalysts.

The morphology of the prepared samples was investigated by SEM and TEM. As shown in Fig. 2a and b, SEM and TEM images of pure  $\text{Ag}_3\text{PO}_4$  were observed to exhibit an approximately spherical morphology that the surface is rough and the particle size is ca. 400–500 nm. PI is shown in Fig. S1a and b as massive laminates formed by stacking. NG is shown in Fig. S1c and d as wrinkled gauze-like flakes. It can be observed that the  $\text{Ag}_3\text{PO}_4$  particles in the  $\text{Ag}_3\text{PO}_4/\text{PI}$  (Fig. S1e and f) and  $\text{Ag}_3\text{PO}_4/\text{NG}$  (Fig. S1g and h) composite photocatalysts are

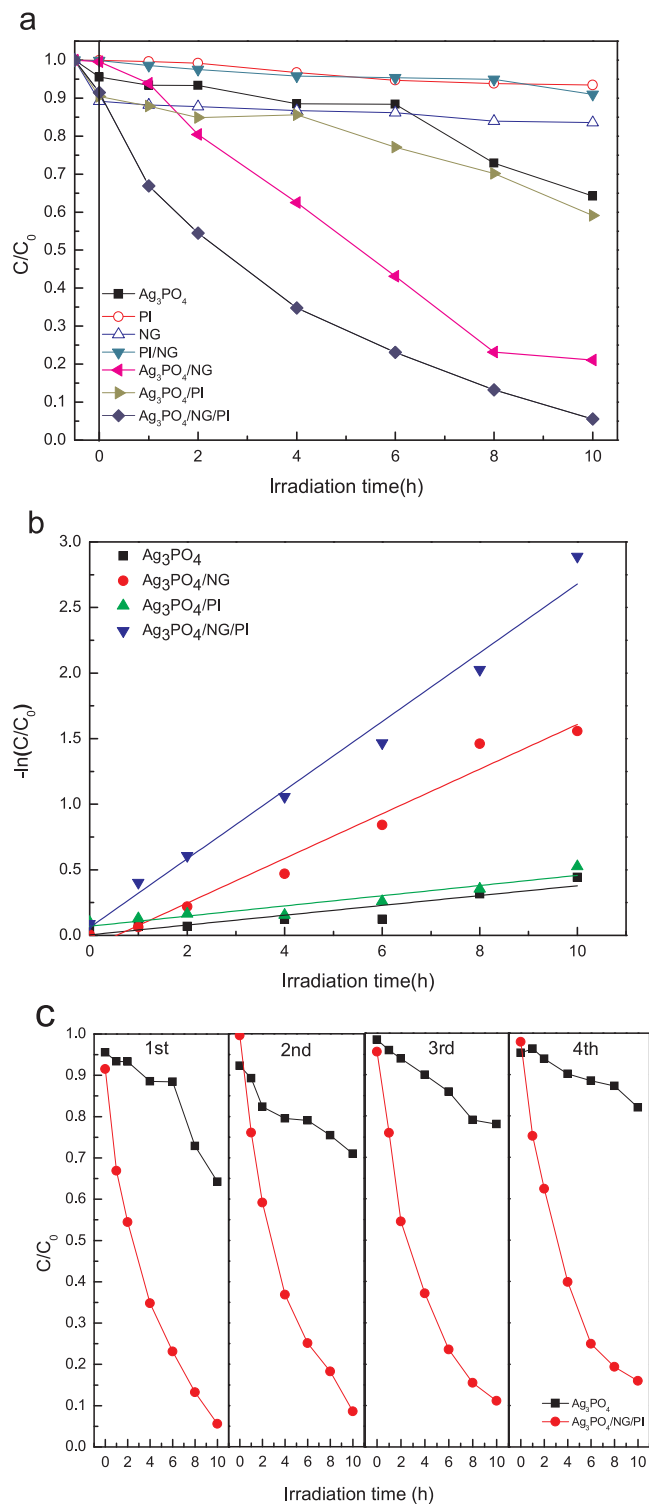


**Fig. 7.** Photocatalytic activities of different samples for MC-LR degradation under visible light irradiation (a), kinetic fit for the photocatalytic degradation of MC-LR with the as-prepared samples (b), cycling tests of  $\text{Ag}_3\text{PO}_4$  and  $\text{Ag}_3\text{PO}_4/\text{NG/PI}$  for photodegradation of MC-LR under visible light irradiation (c).

supported on the surfaces of PI and NG, respectively. In Fig. 2c and d, it can be found that many silver orthophosphate balls are loaded between NG and PI.

The surface composition and chemical state of materials were probed by X-ray photoelectron spectroscopy (XPS). As shown in Supporting information (Fig. S2), it could be seen from the full spectrum of NG (Fig. S2a) that NG exhibited C 1s, N 1s and O 1s

characteristic peaks at 284.1 eV, 400.1 eV and 532.1 eV, respectively. Fig. S2b showed the high resolution N 1s spectrum of NG with two peak positions of 399.1 eV and 400.7 eV, corresponding to pyridinic N and Graphitic N [44]. As shown in Fig. S2c, the C 1s peak of NG was divided into five peaks at 284.1, 284.5, 285.5, 287.4 and 290.7 eV, corresponding to C–C, C=C, C–N, C=O and O–C=O bonds, respectively [45]. The above description indicated that graphene oxide was reduced to graphene by hydrazine hydrate while N atoms were doped into graphene to form nitrogen-doped graphene.

Fig. 3 exhibited the XPS of  $\text{Ag}_3\text{PO}_4/\text{NG/PI}$  composite and  $\text{Ag}_3\text{PO}_4$  photocatalyst. The results showed that the  $\text{Ag}_3\text{PO}_4/\text{NG/PI}$  composite photocatalyst consists of Ag, P, O, C and N. The two characteristic peaks at 367.7 eV and 373.7 eV in Fig. 3f belong to Ag 3d<sub>5/2</sub> and Ag 3d<sub>3/2</sub> respectively, indicating that the valence of the Ag element is +1. Fig. 3e showed that the P 2p peak at 132.3 eV belongs to the binding energy of  $\text{P}^{5+}$  in  $\text{Ag}_3\text{PO}_4$  [46]. The peak of O 1s in Fig. 3d is 530.4 eV and corresponds to the characteristic peak of O element in  $\text{Ag}_3\text{PO}_4$  [23]. Moreover, the C 1s spectra of  $\text{Ag}_3\text{PO}_4/\text{NG/PI}$  composite photocatalyst has two peaks of 284.6 and 288.3 eV, corresponding to C–C/C=C and O–C=O, respectively, as seen in Fig. 3b. The significant increase in the peak of O–C=O at 288.3 eV indicated that PI was successfully combined in  $\text{Ag}_3\text{PO}_4/\text{NG/PI}$  composite photocatalyst [47]. Compared Fig. 3c with Fig. S2b, there is no apparent change in N 1s spectrum. Hence, it can be further concluded that  $\text{Ag}_3\text{PO}_4$ , NG and PI were successfully recombined together.

The result of (FT-IR) (Fig. 4) analysis is consistent with that of XRD. In the (FT-IR) spectrum of  $\text{Ag}_3\text{PO}_4$ , two peaks at  $1010\text{ cm}^{-1}$  and  $558\text{ cm}^{-1}$  are attributed to P–O stretching vibration in  $\text{PO}_4^{3-}$  [48]. For NG, the infrared peaks at  $1380\text{ cm}^{-1}$  belong to the vibrations of carbon–nitrogen bonds [49], indicating that nitrogen atoms have doped into the structure of graphene. Correspondingly, the apparent peak of nitrogen is also found in XRD pattern. As shown in the spectrum of PI, the band at  $1376\text{ cm}^{-1}$  is the C–N stretching vibration absorption peak of the pentahedral imide ring, while the bands at  $1725\text{ cm}^{-1}$ ,  $1772\text{ cm}^{-1}$  and  $725\text{ cm}^{-1}$  are asymmetric secondary shrinkage, symmetrical stretching and bending vibration on the five-membered imide ring absorption peak [50]. The intensities of these absorption peaks of  $\text{Ag}_3\text{PO}_4$  for binary and triple photocatalysts remained essentially unchanged, which was consistent with the results of XRD. It also indicates that the introduction of PI and NG does not alter the structure of  $\text{Ag}_3\text{PO}_4$ .

The electronic structure analyses of  $\text{Ag}_3\text{PO}_4$ ,  $\text{Ag}_3\text{PO}_4/\text{PI}$ ,  $\text{Ag}_3\text{PO}_4/\text{NG}$  and  $\text{Ag}_3\text{PO}_4/\text{NG/PI}$  were probed by the ultraviolet-vis diffuser reflectance spectroscopy (UV-vis DRS). It can be observed from Fig. 5a that there is an obvious absorption band at wavelength of less than 530 nm for  $\text{Ag}_3\text{PO}_4$  in the visible light region. The absorption intensities of  $\text{Ag}_3\text{PO}_4/\text{PI}$ ,  $\text{Ag}_3\text{PO}_4/\text{NG}$  and  $\text{Ag}_3\text{PO}_4/\text{NG/PI}$  composites become stronger in the whole light region, especially in the ultraviolet region. The absorption intensities of the composites are stronger than that of silver orthophosphate at the range of 400–800 nm except that  $\text{Ag}_3\text{PO}_4/\text{PI}$  is slightly decreased at the range of 480–800 nm. As expected, the absorption intensity of  $\text{Ag}_3\text{PO}_4/\text{NG/PI}$  is increased in the whole visible light region. The strengthened photo-absorption of the composites could be attributed to the presence of GO and PI that reduces the reflection of light. Therefore, it can be inferred that the introduction of NG and PI would facilitate the enhancement of the visible light absorbance and the separation of the photogenerated charge of the composite, resulting in enhanced photocatalytic activity of the composite. The valence band energy of the semiconductor was calculated by the Kubelka-Munk formula as shown in Fig. 5b. The band gap of PI,  $\text{Ag}_3\text{PO}_4$  and  $\text{Ag}_3\text{PO}_4/\text{NG/PI}$  composite photocatalysts are  $\sim 2.78\text{ eV}$ ,  $\sim 2.38\text{ eV}$ ,  $\sim 1.92\text{ eV}$ , respectively. As a result,  $\text{Ag}_3\text{PO}_4$  combined with NG and PI reduces the band gap of the photocatalyst, which expanding the optical absorption range of  $\text{Ag}_3\text{PO}_4$ .

Fig. 6 presents the PL emission spectra of  $\text{Ag}_3\text{PO}_4$ ,  $\text{Ag}_3\text{PO}_4/\text{PI}$ ,  $\text{Ag}_3\text{PO}_4/\text{NG}$  and  $\text{Ag}_3\text{PO}_4/\text{NG/PI}$  composites. The PL peaks of these photocatalysts appear at 522 nm. The lower PL intensity indicates the

Table 1

Comparison of different  $\text{TiO}_2$  photocatalysts for MC-LR degradation.

Catalyst name	Catalyst dosage	Initial MC-LR concentration	Light source	Irradiation time	Removal ratio	Refs.
N,P- $\text{TiO}_2$ /EGC	2 g/L	2 mg/L	500 W Xe lamp with a UV cutoff filter ( $\lambda > 385$ nm)	9 h	99.4%	[42]
C- $\text{TiO}_2$	0.2 g/L	2 mg/L	150 W Xe lamp with a 435 nm cutoff filter	5 h	55%	[52]
N- $\text{TiO}_2$	0.25 g/L	2 mg/L	500 W halogen lamp with a UV cutoff filter ( $\lambda > 420$ nm)	10 h	80%	[53]
S- $\text{TiO}_2$	0.23 g/L	0.5 mg/L	Two 15 W fluorescent lamps with a UV block filter (UV420)	5 h	60%	[54]

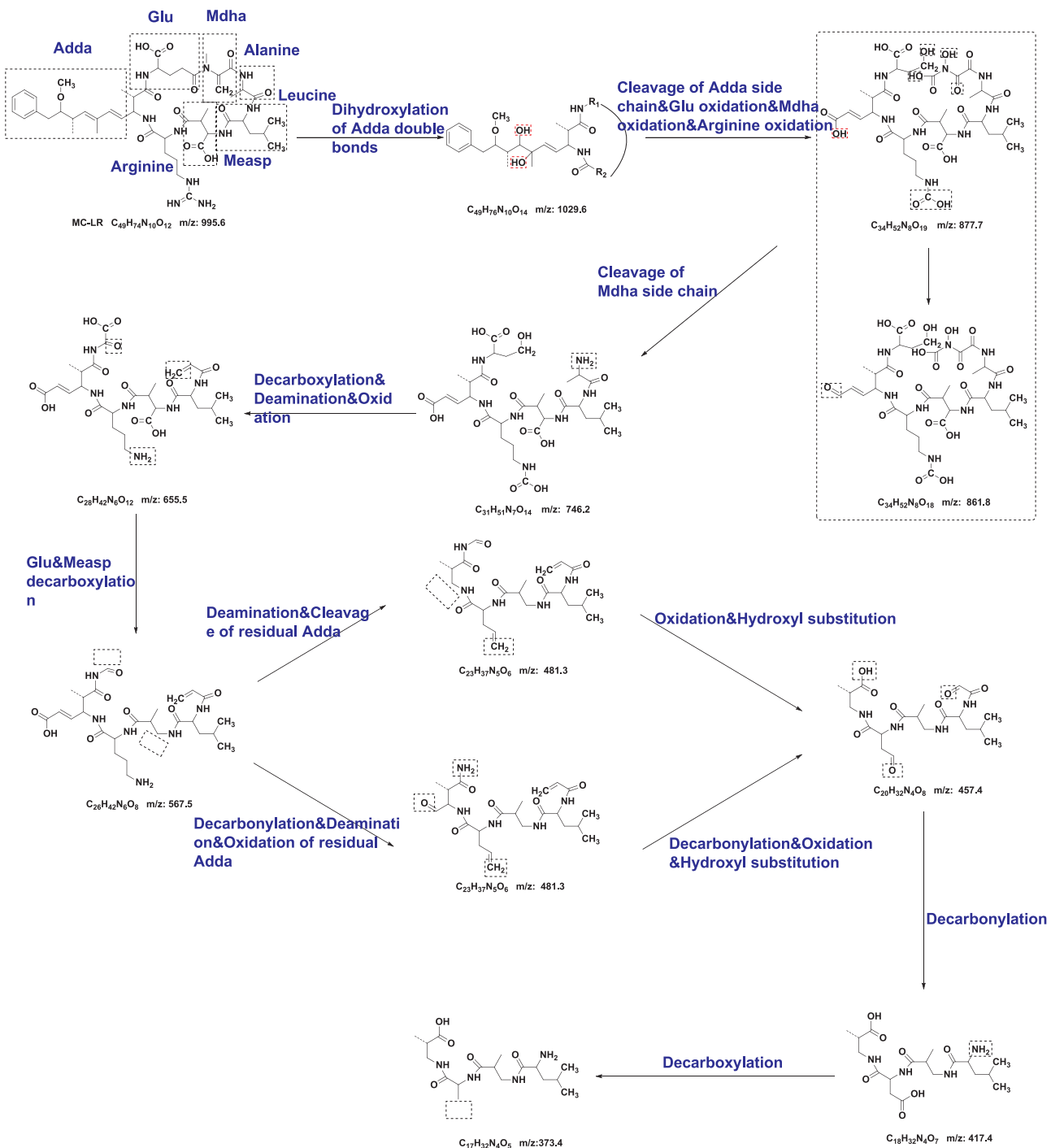


Fig. 8. The possible degradation pathway of MC-LR during the photocatalytic process.

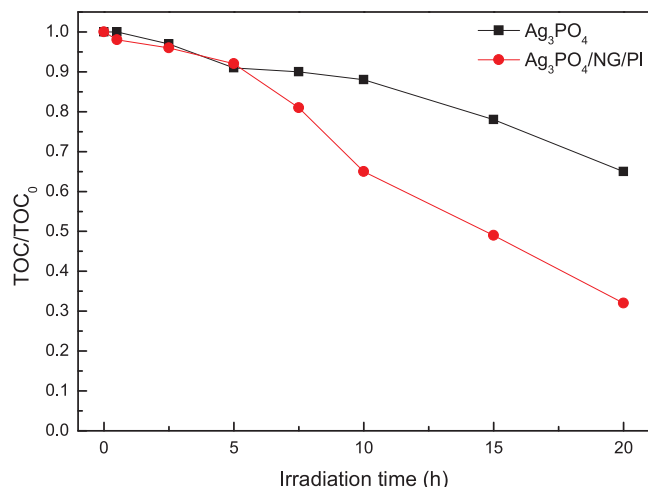


Fig. 9. TOC removal obtained with  $\text{Ag}_3\text{PO}_4$  and  $\text{Ag}_3\text{PO}_4/\text{NG/PI}$  ( $\text{C}_0 = 5 \text{ mg/L}$ ,  $\text{Ag}_3\text{PO}_4/\text{NG/PI} = 0.5 \text{ g/L}$ ,  $T=20^\circ\text{C}$ ,  $P=250 \text{ W}$ ).

lower recombination of the photogenerated electron-hole pairs [28]. Compared with pure  $\text{Ag}_3\text{PO}_4$ , the PL intensity of  $\text{Ag}_3\text{PO}_4$ -based composite photocatalyst is obviously decreased, which indicates that the hybridization of NG and PI can effectively improve the charge separation efficiency and enhance the photocatalytic activity of photocatalyst.

### 3.2. Photocatalytic degradation of MC-LR

The photocatalytic activity of the prepared photocatalyst was studied by using MC-LR as the target contaminant. As shown in Fig. 7a,  $\text{Ag}_3\text{PO}_4$ -based photocatalyst had better photocatalytic activity for MC-LR degradation than  $\text{Ag}_3\text{PO}_4$ , PI and NG. The degradation of MC-LR using  $\text{Ag}_3\text{PO}_4/\text{NG/PI}$ ,  $\text{Ag}_3\text{PO}_4/\text{NG}$ ,  $\text{Ag}_3\text{PO}_4/\text{PI}$  and  $\text{Ag}_3\text{PO}_4$  reached 94.4%, 78.9%, 40.9% and 35.8% for 10 h under visible light irradiation, respectively. It can be confirmed that the hybridization of  $\text{Ag}_3\text{PO}_4$ , NG and PI is favorable for improving the photocatalytic activity of  $\text{Ag}_3\text{PO}_4$ . The photocatalytic degradation of MC-LR shown in Fig. 7b fits for the first-order kinetics model. The Langmuir-Hinshelwood equation [51] can be utilized to calculate the first-order degradation kinetic constant  $k$ . The  $k$  value over  $\text{Ag}_3\text{PO}_4$ ,  $\text{Ag}_3\text{PO}_4/\text{PI}$ ,  $\text{Ag}_3\text{PO}_4/\text{NG}$  and  $\text{Ag}_3\text{PO}_4/\text{NG/PI}$  were calculated to be  $0.037 \text{ h}^{-1}$ ,  $0.038 \text{ h}^{-1}$ ,  $0.170 \text{ h}^{-1}$  and  $0.261 \text{ h}^{-1}$ , respectively. Noticeably, the kinetic constant  $k$  over  $\text{Ag}_3\text{PO}_4/\text{NG/PI}$  was  $\sim 7$  times of pure  $\text{Ag}_3\text{PO}_4$ , which indicates that the introduction of PI and NG into  $\text{Ag}_3\text{PO}_4$  can dramatically accelerate the photocatalytic degradation of MC-LR under visible light irradiation. Meanwhile, the specific surface area ( $S_{\text{BET}} = 12.18 \text{ m}^2 \text{ g}^{-1}$ ) of  $\text{Ag}_3\text{PO}_4/\text{NG/PI}$  composite is larger than that of  $\text{Ag}_3\text{PO}_4$  ( $S_{\text{BET}} = 2.57 \text{ m}^2 \text{ g}^{-1}$ ) because of the introduction of high surface area NG, which provides more active sites to  $\text{O}_2$ ,  $\text{H}_2\text{O}$  and MC-LR.

Table 1 lists the photocatalytic degradation of MC-LR by several  $\text{TiO}_2$  photocatalysts. Compared with the  $\text{TiO}_2$  photocatalysts, the as-prepared  $\text{Ag}_3\text{PO}_4/\text{NG/PI}$  photocatalyst has the advantages in the aspect of catalyst dosage, energy consumption and degradation efficiency, indicating that the visible-light photocatalytic activity of  $\text{Ag}_3\text{PO}_4/\text{NG/PI}$  is highly efficient. The photocatalytic stability of  $\text{Ag}_3\text{PO}_4/\text{NG/PI}$  and  $\text{Ag}_3\text{PO}_4$  investigated by cycling photocatalytic experiments (shown in Fig. 7c) also confirmed the higher stability of  $\text{Ag}_3\text{PO}_4/\text{NG/PI}$  composites.

### 3.3. Reaction intermediates and possible degradation pathway of MC-LR

The degradation products were identified based on the total ion chromatogram (TIC) and  $[\text{M}+\text{H}]^+$   $m/z$  data (Supporting information, Fig. S3). In order to identify the product from the impurity, the criterion for the product peak identification is as follows: the peaks with a signal-

to-noise ratio greater than three can be considered the product peak, or the relative peak area at 0 min increased by  $\sim 2$  times [43]. Some useful products whose mass changes are crucial to infer the chemical structure of unknown MC-LR intermediates are selected from the MS spectrum. For example, if the two products differ in mass by 16, then one can deduce the hydroxylation (+16 Da) of the smaller mass of product. In addition, the phenyl ring cannot be the site of attack if a loss of 134 Da occurs (for example,  $m/z$  from 995.6 to 861.8), because a neutral loss caused by the rearrangement of the ring and methoxy groups produces 134 Adda molecules. According to the criterion, eleven degradation products ( $m/z = 1029.6$ ,  $877.7$ ,  $861.8$ ,  $746.2$ ,  $655.5$ ,  $567.5$ ,  $481.3$ (containing two intermediates),  $457.4$ ,  $417.4$ ,  $373.4$ ) were identified by the MS spectrum corresponding to the product peak. Among of them, the intermediates of  $m/z$  1029.6,  $746.2$ ,  $481.3$ ,  $457.4$  and  $417.4$  have been reported on photocatalytic degradation of MC-LR [42,43,52]. The molecular weight of different products is deduced based on the  $[\text{M}+\text{H}]^+$   $m/z$  of the corresponding molecular ion.

MC-LR consisting of 7 amino acids, 3-amino-9-methoxy-2, 6, 8-trimethyl-10-phenyl-4, 6-decadienoic acid (Adda), iso-glutamic acid (Glu), methyl dehydroalanine (Mdha), d-alanine (Ala), L-leucine (Leu), d-methylaspartic acid (MeAsp), and L-arginine (Arg) can be expressed as Cyclo[-Adda-Glu-Mdha-Ala-Leu-MeAsp-Arg-] [52]. MC-LR isomers with  $m/z$  1029.6 are generated by hydroxyl radical attack at the di-hydroxylation of  $\text{C}=\text{C}$  in the Adda side chain [Adda(OH)<sub>2</sub>], resulting in double hydroxylation of MC-LR. A further pathway for opening the peptide ring has been deduced and the dihydroxylated MC-LR was further oxidized after cutting off the Adda side chain to disengage Mdha, as evidenced by the observation of cleavage products with  $m/z$  877.7 and 861.8. Especially, the pathways of the Adda cleavage shows the loss of MC-LR toxicity during the photocatalytic process by  $\text{Ag}_3\text{PO}_4/\text{NG/PI}$  composites. Among them, the product with  $m/z$  877.7 can be dehydroxylated to remove a hydroxyl group to get the product with  $m/z$  861.8. Then the product with  $m/z$  877.7 was converted to the product with  $m/z$  746.2 by cleavage of Mdha side chain. After further oxidation of Glu and deamination of Alanine as well as decarboxylation of Arginine, peaks with  $m/z$  655.5 also appeared in MS spectrum. The product with  $m/z$  567.5 was observed during the photocatalytic process, which can be achieved via decarboxylation of the Glu and Measp. A series of reactions, such as the oxidation of the residual Adda, deamination, decarbonylation and hydroxyl substitution occurred with the emergence of  $m/z$  481.3 and 457.4 successively. Finally, the products of  $m/z$  417.4 and 373.4 were obtained in turn after decarbonylation of Alanine and decarboxylation of Arginine respectively. The degradation pathway of MC-LR during the photocatalytic process was shown in Fig. 8. From the above analysis, the degradation pathway of MC-LR under the visible light by  $\text{Ag}_3\text{PO}_4/\text{NG/PI}$  composites is significantly different from other photocatalysts reported in previous literature [42,43,52]. The achieved relatively smaller molecular mass of the final degradation product confirms the stronger mineralization ability of  $\text{Ag}_3\text{PO}_4/\text{NG/PI}$  composites for MC-LR.

The mineralization degree of MC-LR was measured by TOC and shown in Fig. 9. The TOC removal ratios of  $\text{Ag}_3\text{PO}_4/\text{NG/PI}$  and  $\text{Ag}_3\text{PO}_4$  reached 35%, 12% at 10 h, and 68%, 35% at 20 h, respectively, indicating the better photocatalytic mineralization of  $\text{Ag}_3\text{PO}_4/\text{NG/PI}$  for MC-LR. According to the analysis of degradation pathway in Fig. 8, the aromatic ring in the molecular structure of MC-LR was firstly degraded and subsequently the generated more stable chain compound was continuously degraded. The degradation products can be speculated to be  $\text{C}_{28}\text{H}_{42}\text{N}_6\text{O}_{12}$  ( $m/z$  655.5) at 10 h, and  $\text{C}_{17}\text{H}_{32}\text{N}_4\text{O}_5$  ( $m/z$  373.4) at 20 h of MC-LR degradation by  $\text{Ag}_3\text{PO}_4/\text{NG/PI}$ .

3.4. Photocatalytic mechanism

To investigate the photocatalytic mechanism, the active species involved in the degradation of MC-LR were first detected by radical trapping experiments, as shown in Fig. 10a. The degradation ratio of MC-LR decreased by 62.4% after adding EDTA-2Na ( $\text{h}^+$  scavenger), decreased by 29.5% after adding BQ ( $\cdot\text{O}_2^-$  scavenger), and was a weak

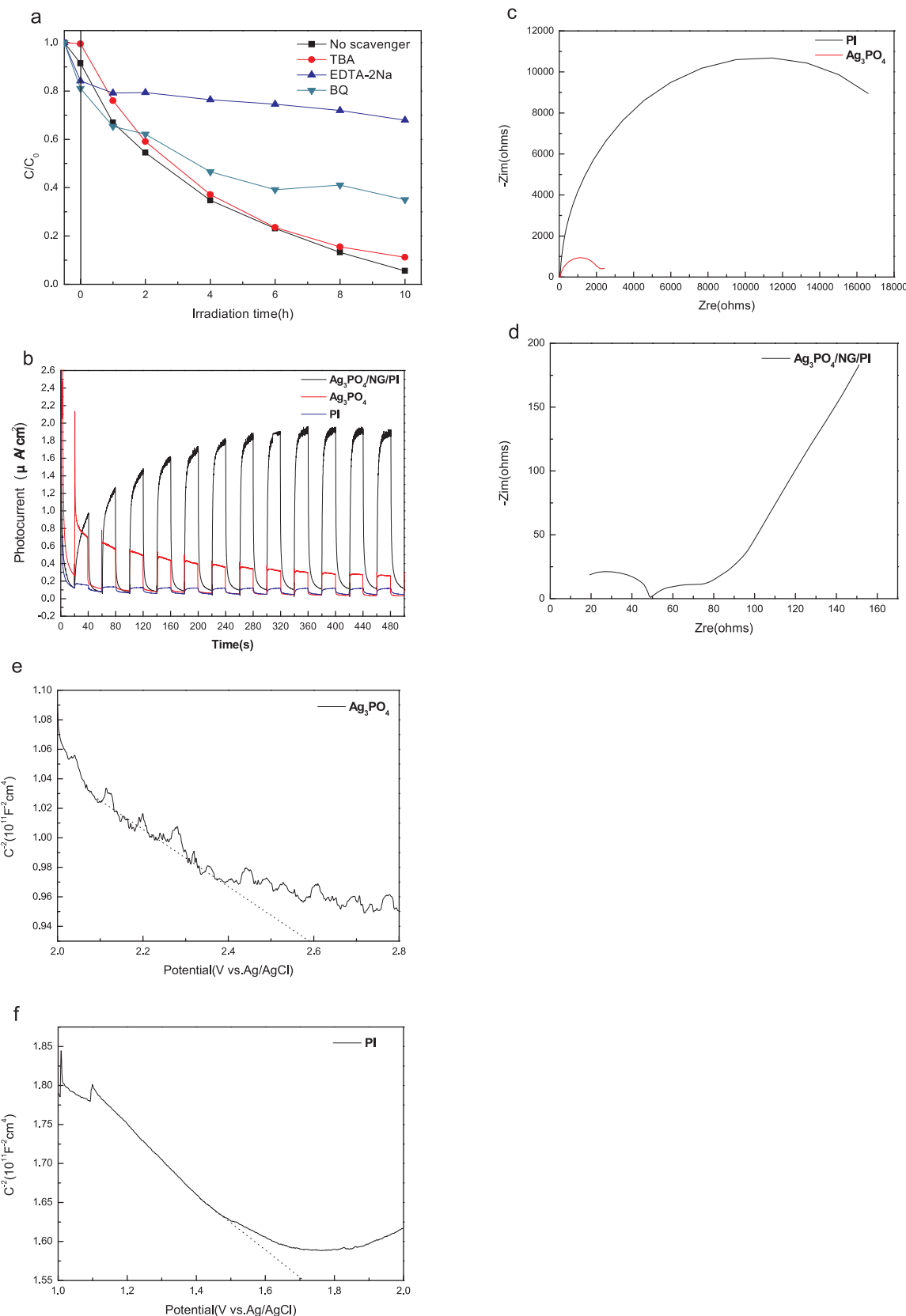


**Fig. 10.** (a) radical trapping experiments of  $\text{Ag}_3\text{PO}_4/\text{NG/PI}$  under visible light irradiation; (b) photocurrent response curve of  $\text{Ag}_3\text{PO}_4$ , PI and  $\text{Ag}_3\text{PO}_4/\text{NG/PI}$ ; (c) EIS of PI and  $\text{Ag}_3\text{PO}_4$ ; (d) EIS of  $\text{Ag}_3\text{PO}_4/\text{NG/PI}$ ; (e) Mott-Schottky plots of  $\text{Ag}_3\text{PO}_4$ ; (f) Mott-Schottky plots of PI.

inhibition by the addition of TBA ( $\cdot\text{OH}$  scavenger). The results demonstrated that photogenerated holes ( $\text{h}^+$ ) was the main active species, and  $\cdot\text{OH}$  made very small contribution to the photocatalytic

reaction.

Fig. 10b showed that the initial photocurrent density of  $\text{Ag}_3\text{PO}_4$  was  $0.8 \mu\text{A cm}^{-2}$ , but its photocurrent density decayed rapidly and

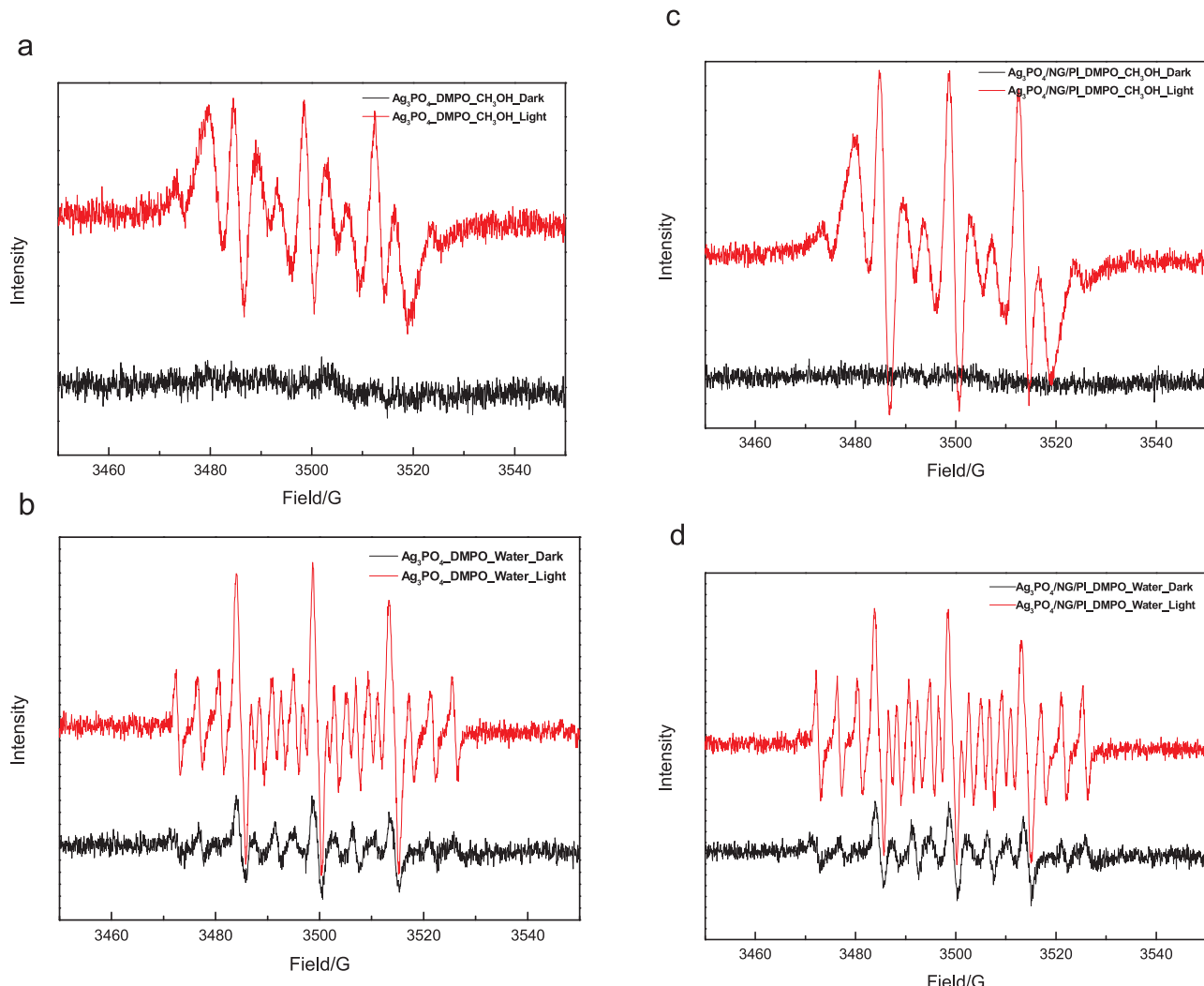


Fig. 11. ESR spectra of (a) DMPO-·O<sub>2</sub><sup>-</sup> adducts of Ag<sub>3</sub>PO<sub>4</sub>, (b) DMPO-·OH adducts of Ag<sub>3</sub>PO<sub>4</sub>, (c) DMPO-·O<sub>2</sub><sup>-</sup> adducts of Ag<sub>3</sub>PO<sub>4</sub>/NG/PI, and (d) DMPO-·OH adducts of Ag<sub>3</sub>PO<sub>4</sub>/NG/PI before and after visible light irradiation.

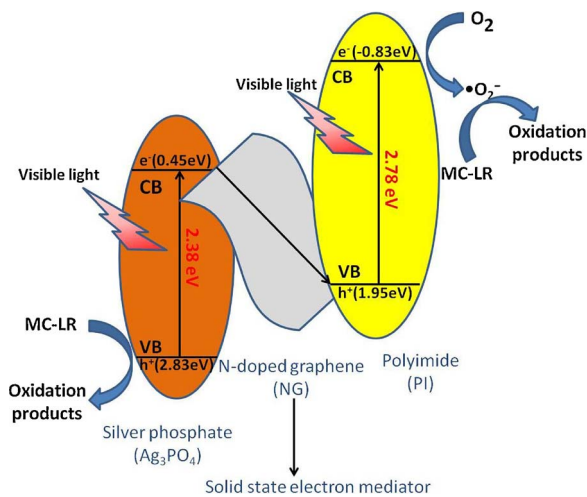


Fig. 12. Z-scheme photocatalytic mechanism for MC-LR degradation using Ag<sub>3</sub>PO<sub>4</sub>/NG/PI composites under visible light irradiation.

decreased to 0.3  $\mu\text{A cm}^{-2}$  after 500 s, which indicates that Ag<sub>3</sub>PO<sub>4</sub> was unstable under visible light ( $\lambda > 420 \text{ nm}$ ). The photocurrent density of PI was 0.15  $\mu\text{A cm}^{-2}$ , and it was still stable under visible light within 500 s. The photocurrent density of Ag<sub>3</sub>PO<sub>4</sub>/NG/PI composites was

2  $\mu\text{A cm}^{-2}$ , which was 2.5 times that of Ag<sub>3</sub>PO<sub>4</sub> and far exceeded the sum of Ag<sub>3</sub>PO<sub>4</sub> and PI. It suggests that there was a synergistic effect between Ag<sub>3</sub>PO<sub>4</sub> and PI to significantly enhance the photoelectric response intensity and effectively inhibit the photo-corrosion. It was also observed that the photoluminescence intensity of Ag<sub>3</sub>PO<sub>4</sub>/NG/PI (Fig. 6) was weakened due to the introduction of PI and NG to increase the separation of photogenerated electron-hole pairs caused by the charge transport between Ag<sub>3</sub>PO<sub>4</sub> and PI, thereby improving the photocatalytic performance of Ag<sub>3</sub>PO<sub>4</sub>/NG/PI.

EIS is a powerful tool for studying a material's electrochemical conductivity properties. The EIS Nyquist plots of the materials shown in Fig. 10c and d were measured in the frequency range of 10<sup>6</sup>–0.1 Hz with amplitude of 5 mV at a bias potential of 0 V versus Ag/AgCl. The impedance of the EIS Nyquist plots is the impedance of the FTO/catalyst, catalyst/electrolyte and catalyst/catalyst interface. The lower the impedance is, the higher the efficiency of the photogenerated carrier separation and the lower the interface resistance are. The minimum interfacial impedance ( $\sim 50 \Omega$ ) of Ag<sub>3</sub>PO<sub>4</sub>/NG/PI composite implies that the composite has better electron transport capability and higher photogenerated carrier separation efficiency than Ag<sub>3</sub>PO<sub>4</sub> or PI alone [53,54]. From the above photoelectrochemical analysis, it can be deduced that the photocatalytic activity and stability of Ag<sub>3</sub>PO<sub>4</sub>/NG/PI composite are derived from its stable and efficient photoelectric conversion property, excellent photogenerated carrier separation efficiency and electron transport capability.

The Mott-Schottky spectrum was employed to determine the flat-band position of samples as shown in Fig. 10e and f. The positive slope of the straight lines indicates that  $\text{Ag}_3\text{PO}_4$  and PI are the *p*-type semiconductors, whose lowest potential of the VB can be approximately estimated to equate with the flat-band potential. The flat-band potentials of  $\text{Ag}_3\text{PO}_4$  and PI are measured to be 2.59 eV and 1.71 eV (vs. SCE), corresponding to 2.83 eV and 1.95 eV (vs. NHE) [26,55], respectively. The difference between the flat-band potential of the semiconductor and the valence band or conduction band potential is 0–0.1 eV [24,54,56], so the valence bands of  $\text{Ag}_3\text{PO}_4$  and PI are ~2.83 eV and ~1.95 eV, respectively. According to the DRS, the band gaps of  $\text{Ag}_3\text{PO}_4$  and PI are ~2.38 eV and ~2.78 eV, thus the conduction bands of  $\text{Ag}_3\text{PO}_4$  and PI are 0.45 eV and –0.83 eV, respectively. Compared to the  $\cdot\text{OH}/\text{H}_2\text{O}$  potential (2.27 V), the VB level of PI is not positive enough to drive the oxidation process of  $\text{H}_2\text{O}$  to form  $\cdot\text{OH}$ . As is well known,  $\text{Ag}_3\text{PO}_4$  can oxidize  $\text{H}_2\text{O}$  to  $\cdot\text{OH}$  and cannot reduce the absorbed  $\text{O}_2$  to yield  $\cdot\text{O}_2^-$  [26] because the CB level of  $\text{Ag}_3\text{PO}_4$  is less negative than the  $\cdot\text{O}_2^-/\text{O}_2$  potential (–0.28 V). ESR experiments were carried out to determine the  $\cdot\text{O}_2^-$  and  $\cdot\text{OH}$  produced during the degradation of MC-LR according to Chen's method [57]. A significant signal of  $\cdot\text{O}_2^-$  was found in Fig. 11a for pure  $\text{Ag}_3\text{PO}_4$  due to the self-decomposition of DMPO. Meanwhile, the characteristic peaks of the DMPO- $\cdot\text{O}_2^-$  adduct observed in the ESR diagram of the  $\text{Ag}_3\text{PO}_4/\text{NG}/\text{PI}$  composite confirm the generation of  $\cdot\text{O}_2^-$ . These observations imply a different transfer route of photogenerated electrons existing in the  $\text{Ag}_3\text{PO}_4/\text{NG}/\text{PI}$  composite photocatalyst.

Herein, a Z-scheme mechanism for the enhanced photocatalytic activity and stability of  $\text{Ag}_3\text{PO}_4/\text{NG}/\text{PI}$  composite is proposed, as illustrated in Fig. 12. Due to their narrow band gaps, both  $\text{Ag}_3\text{PO}_4$  and PI can be easily excited to yield photogenerated electron-hole pairs under visible light irradiation. The photogenerated electrons ( $e^-$ ) in the CB of  $\text{Ag}_3\text{PO}_4$  can be migrated via NG as a solid-state electron mediator and recombined with holes ( $h^+$ ) in the VB of PI. Thus, the VB of  $\text{Ag}_3\text{PO}_4$  and the CB of PI accumulated a large number of more active photogenerated  $h^+$  and  $e^-$ , respectively. The photogenerated holes left behind in the VB of  $\text{Ag}_3\text{PO}_4$  can directly eliminate MC-LR while the remained photogenerated electrons ( $e^-$ ) in the CB of PI can yield  $\cdot\text{O}_2^-$  to indirectly eliminate MC-LR. Eventually, MC-LR was degraded via the  $\text{O}_2^-$  and direct  $h^+$  oxidation pathway.

#### 4. Conclusions

In summary, the photocatalytic activity of  $\text{Ag}_3\text{PO}_4/\text{NG}/\text{PI}$  composite photocatalyst under visible light is higher than that of  $\text{Ag}_3\text{PO}_4$  and binary composites, and the kinetic constant of MC-LR degradation for  $\text{Ag}_3\text{PO}_4/\text{NG}/\text{PI}$  is 7 times of pure  $\text{Ag}_3\text{PO}_4$ . The electron-hole recombination of the CB electrons of  $\text{Ag}_3\text{PO}_4$  and the VB holes of PI occurred via NG as a solid-state electron mediator with the aim of the generation of more oxidative holes in the VB of  $\text{Ag}_3\text{PO}_4$  and more reactive  $\cdot\text{O}_2^-$  in the CB of PI. Such a Z-scheme  $\text{Ag}_3\text{PO}_4/\text{NG}/\text{PI}$  composite photocatalyst enables a fast charge separation and migration of photogenerated electron-hole pairs to produce a powerful oxidation and reduction ability during the photocatalytic degradation of MC-LR by  $\text{Ag}_3\text{PO}_4/\text{NG}/\text{PI}$  composite photocatalyst. Simultaneously, the fast transfer of photogenerated electrons from  $\text{Ag}_3\text{PO}_4$  to NG before  $\text{Ag}^+$  is reduced to  $\text{Ag}^\circ$  successfully inhibits the photo-corrosion of  $\text{Ag}_3\text{PO}_4$  and thus improves the stability of the composite. The investigation will enrich the studies of Z-scheme type photocatalysts and inspire the exploration of Ag-based photocatalysts with high photocatalytic activity and stability.

#### Acknowledgments

We acknowledge the financial support from National Natural Science Foundation of China (No. 51578249), the Science & Technology Planning Project of Guangdong Province (No.

2015A020215028), and Natural Science Foundation of Guangdong Province (No. 2016A030313434).

#### Appendix A. Supplementary data

Supplementary material related to this article can be found, in the online version, at doi:<https://doi.org/10.1016/j.apcatb.2018.02.023>.

#### References

- [1] L.X. Pinho, J. Azevedo, Á. Brito, A. Santos, P. Tamagnini, V.J.P. Vilar, V.M. Vasconcelos, A.R.B. Rui, *Chem. Eng. J.* 268 (2015) 144–152.
- [2] M. Pelaez, B. Baruwati, R.S. Varma, R. Luque, D.D. Dionysiou, *Chem. Commun.* 49 (2013) 10118–10120.
- [3] S.M. El-Sheikh, G. Zhang, H.M. El-Hosainy, A.A. Ismail, K.E. O'Shea, P. Falaras, A.G. Kontos, D.D. Dionysiou, *J. Hazard. Mater.* 280 (2014) 723–733.
- [4] J. Sun, H. Fan, B. Nan, S. Ai, *Sep. Purif. Technol.* 130 (2014) 84–90.
- [5] Y. Liu, F. Liang, H. Lu, Y. Li, C. Hu, H. Yu, *Appl. Catal. B: Environ.* 115–116 (2012) 245–252.
- [6] L. Zhang, K.H. Wong, Z. Chen, J.C. Yu, J. Zhao, C. Hu, C.Y. Chan, P.K. Wong, *Appl. Catal. A: Gen.* 363 (2009) 221–229.
- [7] H. Choi, M.G. Antoniou, M. Pelaez, D.L.C. Aa, J.A. Shoemaker, D.D. Dionysiou, *Environ. Sci. Technol.* 41 (2007) 7530–7535.
- [8] P. Chen, L. Zhu, S. Fang, C. Wang, G. Shan, *Environ. Sci. Technol.* 46 (2012) 2345–2351.
- [9] Z. Yi, J. Ye, N. Kikugawa, T. Kako, S. Ouyang, H. Stuartwilliams, H. Yang, J. Cao, W. Luo, Z. Li, *Nat. Mater.* 9 (2010) 559–564.
- [10] V.K. Sharma, T.M. Triantis, M.G. Antoniou, X. He, M. Pelaez, C. Han, W. Song, K.E. O'Shea, A.A.D.L. Cruz, T. Kaloudis, *Sep. Purif. Technol.* 91 (2012) 3–17.
- [11] S.B. Rawal, D.S. Sang, I.L. Wan, *Catal. Commun.* 17 (2012) 131–135.
- [12] T. Wei, X. Li, Q. Zhao, J. Zhao, D. Zhang, *Appl. Catal. B: Environ.* 125 (2012) 538–545.
- [13] W. Liu, S.O. Chemistry, C. Xu, X. Fu, *Mater. Res. Bull.* 48 (2013) 106–113.
- [14] G. Dai, J. Yu, G. Liu, *J. Phys. Chem. C* 115 (2011) 7339–7346.
- [15] P. Amornpitotksuk, S. Suwanboon, *Adv. Powder Technol.* 25 (2014) 1026–1030.
- [16] C. Cui, Y. Wang, D. Liang, W. Cui, H. Hu, B. Lu, S. Xu, X. Li, C. Wang, Y. Yang, *Appl. Catal. B: Environ.* 158–159 (2014) 150–160.
- [17] G. Chen, M. Sun, Q. Wei, Y. Zhang, B. Zhu, B. Du, *J. Hazard. Mater.* 244–245 (2013) 86–93.
- [18] Z. Xiu, H. Bo, Y. Wu, X. Hao, *Appl. Surf. Sci.* 289 (2014) 394–399.
- [19] Z.W. Tong, D. Yang, Y.Y. Sun, Y. Tian, Z.Y. Jiang, *Phys. Chem. Chem. Phys.* 17 (2015) 12199–12206.
- [20] J. Tian, T. Yan, Z. Qiao, L. Wang, W. Li, J. You, B. Huang, *Appl. Catal. B: Environ.* 209 (2017) 566–578.
- [21] Z. Liu, Y. Liu, P. Xu, Z. Ma, J. Wang, H. Yuan, *ACS Appl. Mater. Interfaces* 9 (2017) 20620–20629.
- [22] C. Zhang, K. Yu, Y. Feng, Y. Chang, T. Yang, Y. Xuan, D. Lei, L.L. Lou, S. Liu, *Appl. Catal. B: Environ.* 210 (2017) 77–87.
- [23] W. Liu, M. Wang, C. Xu, S. Chen, X. Fu, *Mater. Res. Bull.* 48 (2013) 106–113.
- [24] X. Zeng, Z. Wang, G. Wang, T.R. Gengenbach, D.T. McCarthy, A. Deletic, J. Yu, X. Zhang, *Appl. Catal. B: Environ.* 218 (2017) 163–173.
- [25] H. Li, W. Tu, Y. Zhou, Z. Zou, *Adv. Sci.* 3 (2016) 1500389.
- [26] D. Xu, B. Cheng, S. Cao, J. Yu, *Appl. Catal. B: Environ.* 164 (2015) 380–388.
- [27] J. Xian, D. Li, C. Jing, X. Li, H. Miao, S. Yu, L. Yu, J. Fang, *ACS Appl. Mater. Interfaces* 6 (2014) 13157–13166.
- [28] X. Li, T. Wan, J. Qiu, H. Wei, F. Qin, Y. Wang, Y. Liao, Z. Huang, X. Tan, *Appl. Catal. B: Environ.* 217 (2017) 591–602.
- [29] K. Iwashina, A. Iwase, Y.H. Ng, R. Amal, A. Kudo, J. Am. Chem. Soc. 137 (2015) 604–607.
- [30] A. Iwase, Y.H. Ng, Y. Ishiguro, A. Kudo, R. Amal, J. Am. Chem. Soc. 133 (2011) 11054–11057.
- [31] P. Zhou, J. Yu, M. Jaroniec, *Adv. Mater.* 26 (2014) 4920–4935.
- [32] A. Iwase, S. Yoshino, T. Takayama, H.N. Yun, R. Amal, A. Kudo, J. Am. Chem. Soc. 138 (2016) 10260–10264.
- [33] K.S. Novoselov, A.K. Geim, S.V. Morozov, D. Jiang, Y. Zhang, S.V. Dubonos, I.V. Grigorieva, A.A. Firsov, *Science* 306 (2004) 666–669.
- [34] X. Li, T. Dai, Y. Ma, S. Han, B. Huang, *Phys. Chem. Chem. Phys.* 16 (2014) 4230–4235.
- [35] D. Wei, Y. Liu, Y. Wang, H. Zhang, L. Huang, G. Yu, *Nano Lett.* 9 (2009) 1752–1758.
- [36] Z. Mou, Y. Wu, J. Sun, P. Yang, Y. Du, C. Lu, *ACS Appl. Mater. Interfaces* 6 (2014) 13798–13806.
- [37] Y. Tian, F. Wang, Y. Liu, F. Pang, X. Zhang, *Electrochim. Acta* 146 (2014) 646–653.
- [38] J.Y. Li, X. Jiang, L. Lin, J.J. Zhou, G.S. Xu, Y.P. Yuan, *J. Mol. Catal. A: Chem.* 406 (2015) 46–50.
- [39] S. Ramasundaram, M.G. Seid, W. Lee, C.U. Kim, E.J. Kim, S.W. Hong, K.J. Choi, *J. Hazard. Mater.* 340 (2017) 300–308.
- [40] Y. Min, G. He, Q. Xu, Y. Chen, *J. Mater. Chem. A* 2 (2013) 1294–1301.
- [41] J. Tang, J. Yang, X. Zhou, G. Chen, J. Xie, *Mater. Lett.* 131 (2014) 340–343.
- [42] X. Wang, X. Wang, J. Zhao, J. Song, L. Zhou, J. Wang, X. Tong, Y. Chen, *Appl. Catal. B: Environ.* 206 (2017) 479–489.
- [43] J. Andersen, C. Han, K. O'Shea, D.D. Dionysiou, *Appl. Catal. B: Environ.* 154–155 (2014) 259–266.
- [44] Q. Mi, D. Chen, J. Hu, Z. Huang, J. Li, *Chin. J. Catal.* 34 (2013) 2138–2145.

- [45] S. Mukherjee, T.P. Kaloni, *J. Nanopart. Res.* 14 (2012) 1–5.
- [46] H. Xu, C. Wang, Y. Song, J. Zhu, Y. Xu, J. Yan, Y. Song, H. Li, *Chem. Eng. J.* 241 (2014) 35–42.
- [47] Z. Pan, T. Wang, L. Chen, S. Idziak, Z. Huang, B. Zhao, *Appl. Surf. Sci.* 416 (2017) 536–546.
- [48] L. Liu, L. Ding, Y. Liu, W. An, S. Lin, Y. Liang, W. Cui, *Appl. Catal. B: Environ.* 201 (2016) 92–104.
- [49] Y. Xu, M. Wu, X.Z. Feng, X.B. Yin, X.W. He, Y.K. Zhang, *Chem.-Eur. J.* 19 (2013) 6282–6288.
- [50] S. Zeng, L. Guo, F. Cui, Z. Gao, J. Zhou, J. Shi, *Macromol. Chem. Phys.* 211 (2010) 698–705.
- [51] Y. Zhang, C. Xie, F.L. Gu, H. Wu, Q. Guo, J. Hazard. Mater. 315 (2016) 23–24.
- [52] T. Fotiou, T.M. Triantis, T. Kaloudis, L.M. Pastranamartínez, V. Likodimos, P. Falaras, A.M.T. Silva, A. Hiskia, *Ind. Eng. Chem. Res.* 52 (2013) 13991–14000.
- [53] F. Deng, F. Zhong, D. Lin, L. Zhao, Y. Liu, J. Huang, X. Luo, S. Luo, D.D. Dionysiou, *Appl. Catal. B: Environ.* 416 (2017) 536–546.
- [54] Y. Gong, X. Quan, H. Yu, S. Chen, *Appl. Catal. B: Environ.* 219 (2017) 439–449.
- [55] J. Shang, W. Hao, X. Lv, T. Wang, X. Wang, Y. Du, S. Dou, T. Xie, D. Wang, J. Wang, *ACS Catal.* 4 (2014) 954–961.
- [56] J. Wang, Y. Yu, L. Zhang, *Appl. Catal. B: Environ.* 136–137 (2013) 112–121.
- [57] S. Chen, L. Ji, W. Tang, X. Fu, *Dalton Trans.* 42 (2013) 10759–10768.